Carbon Energy

WILEY

CARBON ENERGY

RESEARCH ARTICLE OPEN ACCESS

Modulating Redox Mechanism in Metal Chalcogenides by Precisely Controlling Phase Transition to Achieve Ultrafast and Ultra-Stable Sodium-Ion Batteries

Yishun Xie[1,2] | Jinlian Yu[3] | Yameng Fan[4] | Guangchang Yang[1,3] | Feiyan Lai[1,2,3] | Xiaohui Zhang[1,2,3,5,6] | Yu Wang[7] | Jie Wang[5,6] | Weihan Li[5,6] | Changhong Wang[5,6] | Zhenxiang Cheng[8] | Hongqiang Wang[3] | Xin Fan[2] | Jian Peng[5,6]

[1]College of Materials and Chemical Engineering, Guangxi Key Laboratory of Calcium Carbonate Resources Comprehensive Utilization, Hezhou University, Hezhou, China | [2]Key Laboratory of Natural and Biomedical Polymer Materials (Education Department of Guangxi Zhuang Autonomous Region), College of Materials Science and Engineering, Guilin University of Technology, Guilin, China | [3]Guangxi Key Laboratory of Low Carbon Energy Materials, Guangxi New Energy Ship Battery Engineering Technology Research Center, Guangxi Scientific and Technological Achievements Transformation Pilot Research Base of Electrochemical Energy Materials and Devices, School of Chemistry and Pharmaceutical Sciences, Guangxi Normal University, Guilin, China | [4]School of Science, RMIT University, Melbourne, Victoria, Australia | [5]Eastern Institute for Advanced Study, Ningbo Institute of Digital Twin, Eastern Institute of Technology, Ningbo, Zhejiang, China | [6]Zhejiang Key Laboratory of All-Solid-State Battery, Ningbo Key Laboratory of All-Solid-State Battery, Ningbo, Zhejiang, China | [7]Department of Materials, University of Oxford, Oxford, UK | [8]Institute for Superconducting and Electronic Materials, Faculty of Engineering and Information Sciences, University of Wollongong, Innovation Campus, North Wollongong, New South Wales, Australia

Correspondence: Xiaohui Zhang (zxhui017@163.com) | Xin Fan (xfan@glut.edu.cn) | Jian Peng (jpeng@eitech.edu.cn)

Received: 6 September 2025 | **Revised:** 14 October 2025 | **Accepted:** 5 November 2025

Funding: This study was supported by the Guangxi Natural Science Foundation (Grant No. 2024GXNSFAA010515), National Natural Science Foundation of China (grant nos. No. 51964013W2441017, 22409103), and the "Innovation Yongjiang 2035" Key R&D Program (grant nos. 2024Z040, 2025Z063).

Keywords: energy storage mechanism | fast-charging anode | heterogeneous structure | sodium-ion batteries

ABSTRACT

Metal chalcogenides represent promising anodes for sodium-ion batteries due to their high theoretical capacities and low material costs. However, their practical applications are hampered by inherently sluggish ion diffusion kinetics and severe volume expansion associated with their conventional conversion reaction mechanism. Here, we design a micro-nano ZnS/ZnSe heterostructured anode through in situ localized phase transformation strategy. This meticulously engineered architecture effectively modulates the Na^+ storage mechanism from a typical conversion reaction to the surface redox pseudocapacitive reaction by precisely controlling the phase transition processes. Such structural control substantially increases Na^+ diffusion sites and reconstructs internal electric fields. Moreover, abundant heterointerfaces and porous microstructure effectively alleviate internal mechanical stresses, provide a large number of Na^+ storage sites and fast Na^+ migration channels, collectively ensuring ultrafast reaction kinetics and superior structural stability of the ZnS/ZnSe. As a result, the ZnS/ZnSe exhibits a remarkable specific capacity of 796 mAh g^{-1} at 0.1 A g^{-1}, stable cycling with no capacity decay over 1800 cycles at 15 A g^{-1}, and capacity retention of 89% even at ultrahigh current density of 20 A g^{-1}. Furthermore, the practical viability of this material is successfully demonstrated in a $NaNi_{1/3}Fe_{1/3}Mn_{1/3}O_2$(NFM)//ZnS/ZnSe full-cell, which shows outstanding cycling stability without noticeable capacity fading after 600 cycles.

Yishun Xie, Jinlian Yu, and Yameng Fan contributed equally to this article.

1 | Introduction

The rapid advancement of electric vehicles (EVs) signifies a transformative shift in the conventional automotive industry, offering promising solutions to challenges related to energy sustainability and environmental pollution [1–3]. However, the prolonged charging times associated with EVs severely restrict their widespread application. Consequently, developing advanced fast-charging technologies is critically urgent. Sodium-ion batteries (SIBs), benefiting from abundant sodium resources and a lower activation barrier compared to lithium-ion batteries (LIBs), hold considerable promise in addressing these challenges [4, 5]. According to the international standard requiring an 80% state-of-charge within 10–15 min, the electrode materials must demonstrate superior rate performance and cycling stability [6, 7]. Therefore, achieving high electrical conductivity and excellent structural robustness becomes imperative in designing suitable fast-charging anode materials.

Currently, hard carbon remains the most commercially viable anode material for SIBs due to its balanced electrochemical performance. However, intrinsic limitations, such as slow sodium ion migration rates ($< 10^{-4}$ S/cm) and theoretical specific capacity of about 350 mAh g^{-1}, pose significant hurdles for high-rate applications [8, 9]. Titanium-based materials exhibit exceptional cycling stability and rapid charge/discharge capability. However, their low theoretical capacity and inherent poor conductivity limit their suitability for high-energy fast-charging applications. Additionally, alloy-type anode materials possess exceptionally high theoretical capacities and low operating voltages, yet substantial volume changes during cycling severely compromise their structural integrity and cycling stability [10, 11]. Recently, conversion-based materials (TMOs/TMSs/TMSe) have emerged as promising alternatives with significantly higher theoretical capacities [12–14]. Unfortunately, these materials exhibit severe volumetric expansion and limited ionic/electronic conductivity, negatively impairing cycling stability and reversibility during the (de)sodiation process [15, 16]. Therefore, rational multiscale structural engineering is crucial for simultaneously enhancing ion/electron transport kinetics and mechanical stability to improve cycling durability and rate capability.

Among various anode candidates for fast-charging SIBs, metal chalcogenides are promising for their high theoretical capacity and elemental abundance [17, 18]. Metal selenides, in particular, exhibit higher electrical conductivity than metal sulfides, due to their narrower band gap and lower bond energy. These features facilitate more efficient electron transport and reduce the energy barrier for bond cleavage and formation during electrochemical cycling [19, 20]. However, their severe volume expansion under high current densities leads to rapid stress accumulation and structural degradation, limiting long-term stability [21, 22].

To address these issues, pseudocapacitive ion storage has emerged as an effective design strategy for anode materials. Unlike conventional intercalation or conversion processes, pseudocapacitive storage involves surface or near-surface redox reactions with capacitor-like rapid charge/discharge kinetics [23, 24]. This approach effectively mitigates kinetic limitations and structural degradation, enabling rate performance beyond the theoretical limitations of traditional battery materials [25, 26]. Achieving a high pseudocapacitive contribution requires materials with high specific surface area, accessible active sites, and rationally designed pore structures. Further enhancement can be achieved by constructing heterostructures with precisely coupled semiconductor interfaces, which create built-in electric fields and reduce ion migration barriers, enhancing charge transfer and structural stability [27, 28]. Such heterostructures can be engineered via controlled in situ phase transformation, achieving the structural robustness and superior conductivity in metal chalcogenides, thereby maximizing pseudocapacitive contributions [29, 30]. In this context, Zn-based chalcogenides are especially attractive due to their morphological and structural tunability, high theoretical specific capacity, and low cost [31, 32]. However, their practical application remains limited by the inherent low conductivity, slow Na^+ diffusion kinetics, and structural collapse during cycling. Precise structural control through regulation of external morphology and internal crystal arrangement has been reported to improve reaction kinetics and structural stability [33, 34]. Despite these advances, a synergistic strategy that combines architectural design with heterointerface engineering for rapid pseudocapacitive Na^+ storage in Zn-based anodes remains unexplored.

In this study, porous spherical ZnS/ZnSe heterostructure anode material was synthesized by in situ localized phase transformation, tailored specifically for fast-charging SIBs. The typical conversion reaction mechanism of ZnS/ZnSe was successfully modulated toward surface redox pseudocapacitive reaction by capitalizing on the synergistic interplay between the heterointerface and porous structure. The unique spherical porous architecture of ZnS/ZnSe heterostructure establishes an intrinsic electric field that simultaneously reduces Na^+ diffusion energy barriers and enhances electron transfer kinetics, while its spherical morphology with porosity significantly shortens both ionic and electronic transport pathways. Importantly, the porous spherical structure effectively buffers volume distortion, maintaining structural integrity during repeated discharge/charge cycles. Consequently, the ZnS/ZnSe heterostructure exhibits superior storage capacity, prolonged cycling lifespan, and impressive rate capability, establishing significant potential for practical applications in fast-charging SIBs.

2 | Result and Discussion

Figure 1 presents the synthetic route and corresponding crystal structure of the ZnS/ZnSe heterostructure. Initially, the ZnS precursor was synthesized via a facile hydrothermal method, followed by a controlled selenization process, enabling localized in situ phase conversion to form a porous ZnS/ZnSe heterostructure. An intrinsic built-in electric field spontaneously established at the ZnS/ZnSe interface, effectively enhancing Na^+ diffusion kinetics and simultaneously facilitating efficient charge transfer. The porous structure, characterized by a large surface area, exposes abundant active sites, accommodates sufficient electrolyte, and effectively buffers volume stress during cycling. Moreover, the ZnS/ZnSe heterostructure undergoes structural reconstruction after cycling, optimizing the diffusion path and transforming the Na^+ storage mechanism from a conversion reaction to a surface redox pseudocapacitive reaction.

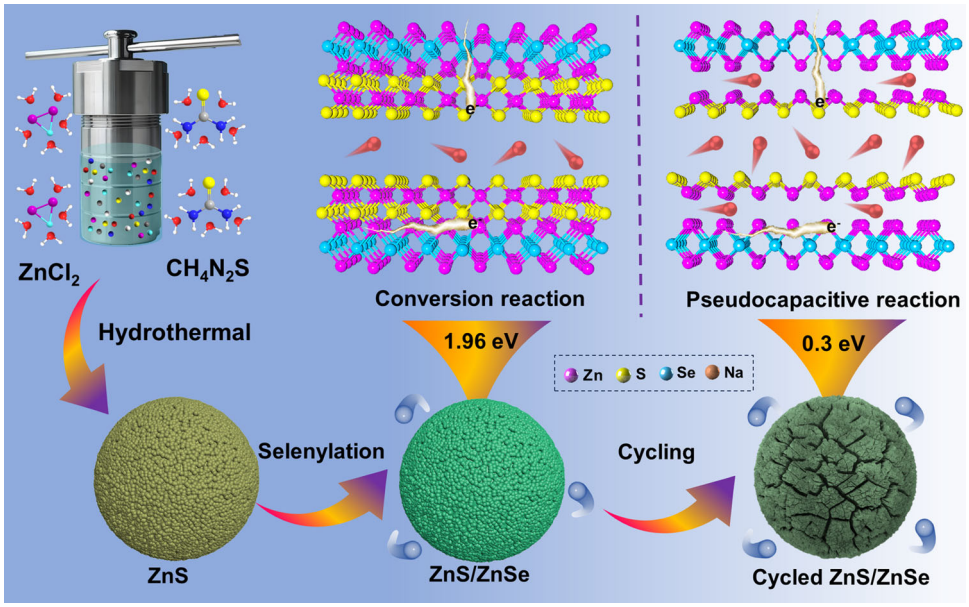

FIGURE 1 | Schematic diagram of the structure design and evolution of the ZnS/ZnSe heterostructure.

The XRD Patterns of ZnS, ZnS/ZnSe, and ZnSe are shown in Supporting Information: Figure S1. All diffraction peaks match well with standard reference patterns of the ZnS (PDF#05-0566) and ZnSe (PDF#37-1463) [35, 36]. Following the selenization, the primary (111) diffraction peak for ZnS is still observable in the ZnS/ZnSe heterostructure, but with remarkably reduced intensity, indicating lattice distortion and interface formation due to partial selenium substitution. Two new peaks at 27.2° and 45.2°, assigned to the (111) and (220) planes of the ZnSe (PDF#37-1463), appear and confirm the successful formation of the ZnS/ZnSe heterostructure [36]. Rietveld refinement shows that the weight ratio of ZnS to ZnSe is 21.5%–78.5% (Supporting Information: Figure S2A). When the selenization temperature reaches 450°C, the diffraction peaks of ZnS entirely disappear, demonstrating the Se substitution of S in the lattice of ZnS. Supporting Information: Figure S2B shows the XPS survey spectra of ZnS/ZnSe, clearly identifying distinct peaks corresponding to Zn 2p, S 2p, and Se 3 d. This confirms the presence of Zn, S, and Se elements within the heterostructure. Quantitative analysis of the XPS spectra suggests an atomic concentration ratio of S:Se = 1:3 (Supporting Information: Table S1). As shown in Supporting Information: Figure S3, the Zn 2p spectrum of ZnS/ZnSe shows two characteristic peaks located at 1044.8 and 1021.6 eV, corresponding to Zn $2p_{1/2}$ and Zn $2p_{3/2}$ orbitals, consistent with previous reports for Zn^{2+} in ZnS and ZnSe [37]. Besides, the S 2p peaks at 162.7 and 161.3 eV associated with S $2p_{1/2}$ and S $2p_{3/2}$ orbital electrons of S^{2-} [38]. The peaks at 55.2 and 54.2 eV are related to the Se $3d_{3/2}$ and Se $3d_{5/2}$ orbital electrons of Se^{2-} [39]. Furthermore, ZnS/ZnSe shows reduced binding energy in the S 2p region and decreased atomic concentration of S compared to pure ZnS (Supporting Information: Figure S3 and Table S1), suggesting the electron transfer from the electron-rich ZnS phase to the electron-deficient ZnSe component. This electron redistribution leads to the formation of a built-in internal electric field at the ZnS/ZnSe heterojunction interface, thereby facilitating enhanced charge transfer processes.

The morphological features and internal structural features of ZnS, ZnS/ZnSe, and ZnSe were systematically investigated by SEM and TEM. As shown in Supporting Information: Figure S4, the ZnS shows uniform spherical particles with a diameter of 10 μm composed of densely aggregated nanoparticles formed via the hydrothermal method. High-magnification SEM images (Figure 2A′) further show a rough surface due to the aggregation of nanoparticles, while Figure 2A″ clearly reveals the presence of numerous interparticle voids within the microspheres. Such porous architectures have previously been shown to enhance the reaction kinetics by increasing the active surface area and facilitating electrolyte penetration, thereby optimizing the active materials utilization and improving rate performance [40, 41]. To further improve the conductivity and Na^+ transport kinetics, the ZnS/ZnSe heterostructure was fabricated by in situ phase transformation process based on the structural advantage of ZnS. After selenization, the ZnS/ZnSe still retained its uniform microsphere but exhibited significantly increased pore density and larger average pore size compared to ZnS (Figure 2B′). Additionally, the ZnS/ZnSe heterostructure exhibits significantly larger average grain size compared to pristine ZnS in Figure 2B″. Brunauer-Emmett-Teller (BET) measurements demonstrate that ZnS/ZnSe possesses a substantially higher specific surface area (26.14 $m^2 g^{-1}$) compared to ZnS (5.68 $m^2 g^{-1}$) and ZnSe (9.99 $m^2 g^{-1}$) as shown in Figure 2J, which provides abundant ion transport channels to facilitate Na^+ diffusion within the bulk material. Furthermore, the TEM image in Figure 2D shows a clear lattice fringe of 0.312 nm, corresponding to the (111) crystal planes of ZnS. The selected area electron diffraction (SAED) pattern is identified to correspond to the (111), (220), and (311) planes of ZnS. In the high-resolution TEM (HRTEM) of ZnS/ZnSe, two types of lattice stripes are clearly visible in Figure 2E. Among them, the obvious lattice fringe observed in the region I can be identified as the (111) crystal planes of ZnS, corresponding lattice spacing of 0.312 nm [42]. Furthermore, the phase with an interplanar spacing of 0.327 nm can be attributed to the (111) planes of ZnSe [43]. Importantly, an obvious phase boundary can be

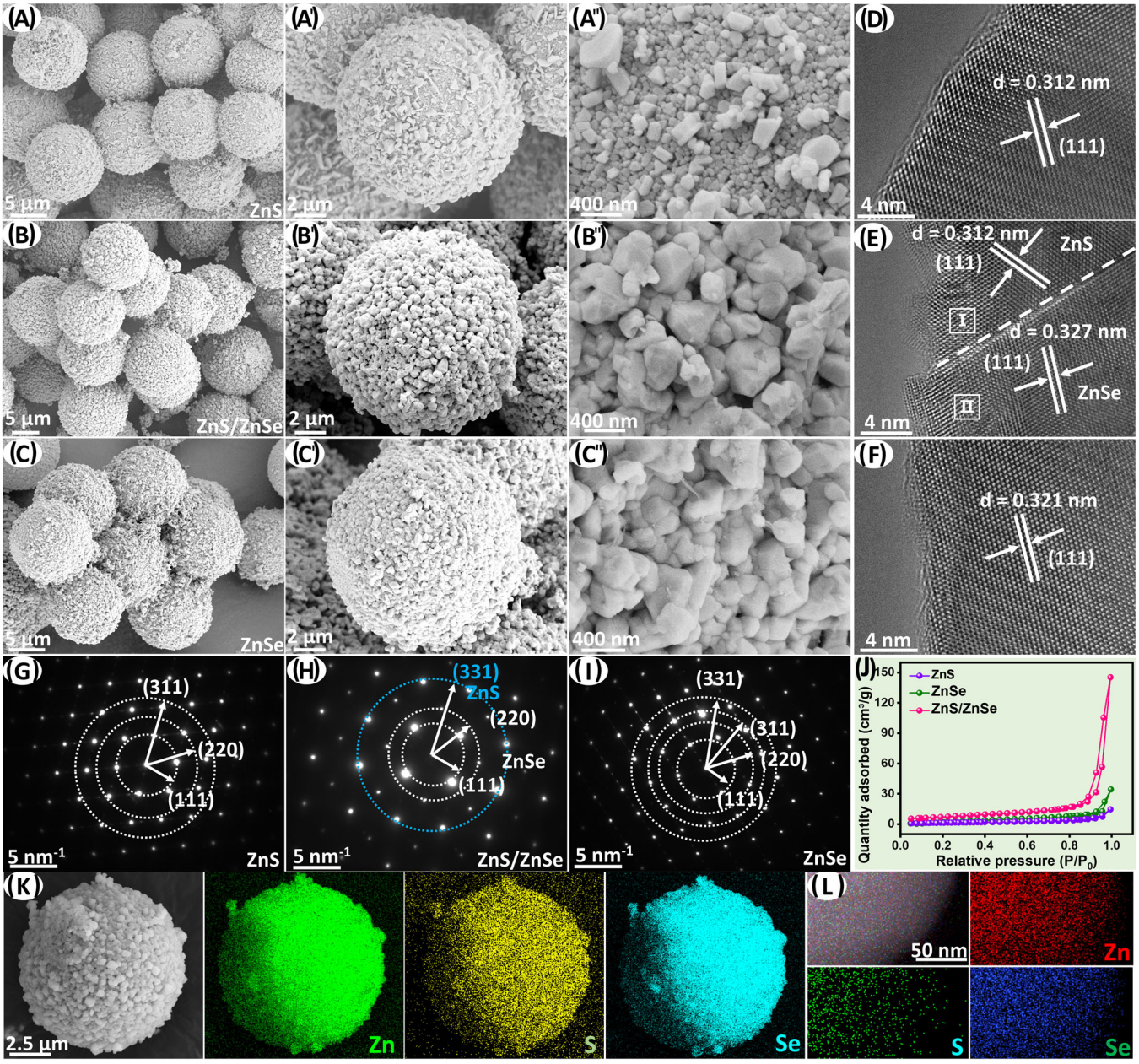

FIGURE 2 | SEM and images of the ZnS (A–A″), ZnS/ZnSe (B–B″), and ZnSe (C–C″). TEM and SAED images (D–I). BET curves (J). The EDS elemental mappings (K, L).

observed in Figure 2E and these findings confirm the successful formation of the ZnS/ZnSe heterostructures through the vapor adsorption/selenization method. It is worth noting that the introduction of heterointerfaces generates abundant defect sites and active interfaces, which significantly enhanced ion and electron diffusion kinetics while effectively mitigating volumetric stresses during cycling, as shown in Supporting Information: Figure S5. The SAED pattern in Figure 2H further confirms that the two white-colored diffraction rings align with the (111) and (220) planes of ZnSe, whereas the blue-colored ring corresponds to the (331) plane of ZnS. Elemental mapping by SEM and TEM-EDS (Figure 2K,L) reveals the uniform distributions of Zn, S, and Se elements, further demonstrating the successful construction of the ZnS/ZnSe heterostructure. Based on the elemental contents shown in Supporting Information: Figure S6, the atomic proportion of S and Se in the heterostructure was determined to be 1:3.6, consistent with XPS analyses. Upon increased selenization, the ZnS/ZnSe progressively transitions into pure ZnSe, which exhibits significantly reduced pore density and smaller pore size (Figure 3C–C″). Moreover, TEM image (Figure 2I) and SAED pattern distinctly confirm the cubic ZnSe phase through clearly showing lattice fringe and four indexed diffraction rings, corresponding to the (111), (220), (311), and (331) planes, highlighting the clear structural evolution associated with increasing selenization levels.

To elucidate the differences in Na^+ storage mechanism between ZnS and ZnS/ZnSe, comparative cyclic voltammetry (CV) and galvanostatic charge-discharge (GCD) analyses were performed.

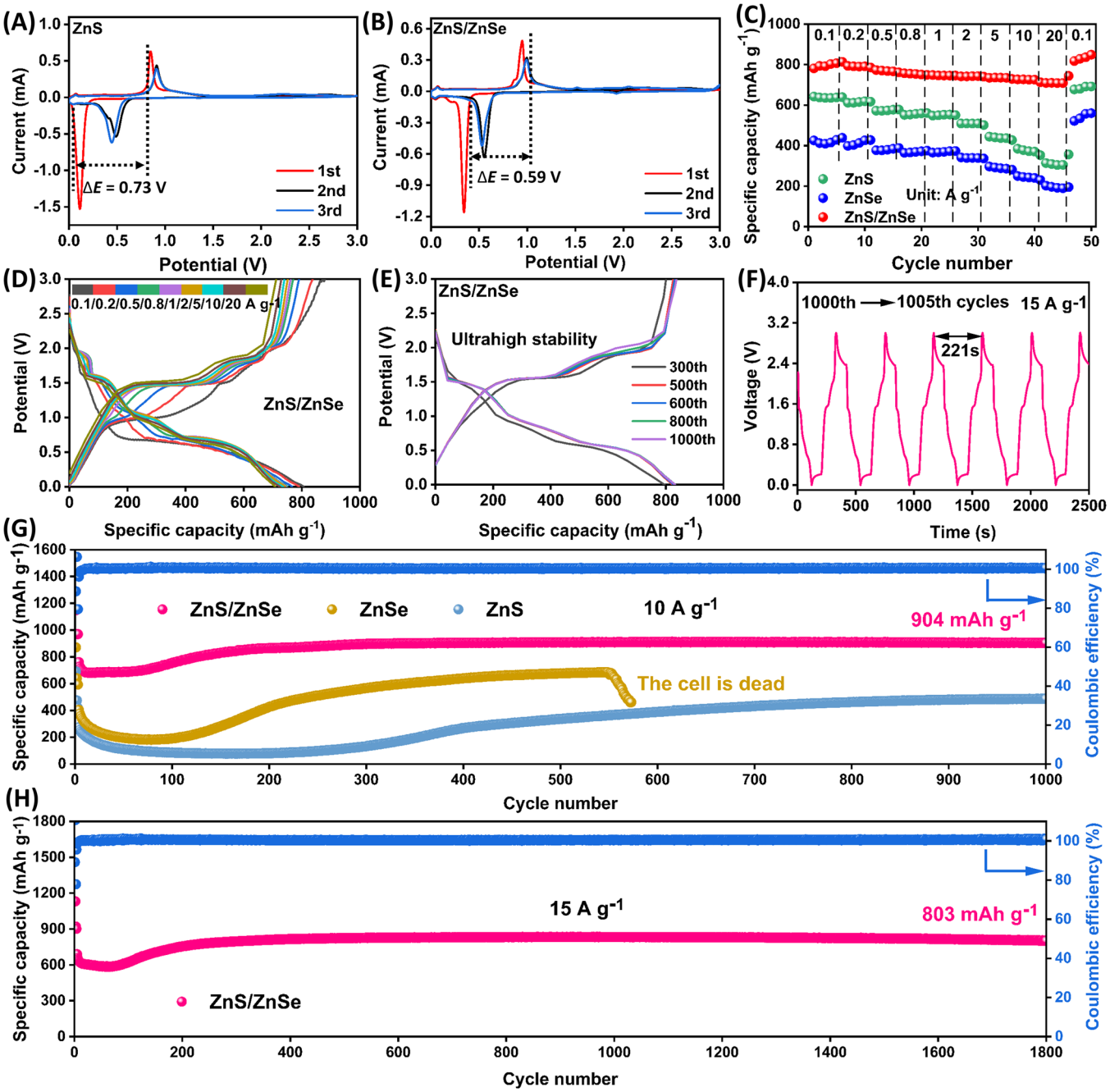

FIGURE 3 | Cyclic voltammetry (CV) curves for ZnS (A) and ZnS/ZnSe (B). Rate capability (C), charge-discharge curves at various current densities (D), and various cycles at 10 A g^{-1} (E). The voltage-time profiles at 15 A g^{-1} (F). Cycling performance at 10 A g^{-1} (G) and 15 A g^{-1} (H) of ZnS/ZnSe.

All samples exhibit paired redox with similar profiles, corresponding to the oxidation and reduction reaction of Zn/Zn^{2+} ($ZnS + 2Na^+ + 2e^- \leftrightarrow Zn + Na_2S$; $ZnSe + 2Na^+ + 2e^- \leftrightarrow Zn + Na_2Se$) [34, 38]. Apart from the cathodic peak at low potentials (~0.11 V and 0.34 V) observed in the initial cycle, the redox curves of the samples exhibit excellent overlap in subsequent cycles. This behavior indicates that irreversible capacity loss primarily results from the formation of the SEI layer and partly originates from the Na^+ during the first charge process. The potential difference ($\Delta E_{OR} = E_O - E_R$) between oxidation and reduction peaks reflects both the reversibility of the electrode reaction and the extent of polarization [44, 45]. In Figure 3B, the ZnS/ZnSe electrode exhibits initial redox peaks located at 0.93 and 0.34 V; therefore, the potential difference of the ZnS/ZnSe ($\Delta E_{OR} = 0.59$ V) is smaller than that of ZnS ($\Delta E_{OR} = 0.73$ V) and ZnSe ($\Delta E_{OR} = 0.62$ V) (Supporting Information: Figure S7). This smaller ΔEOR demonstrates that ZnS/ZnSe possesses higher electrochemical reversibility and faster reaction kinetics due to lower energy loss and reaction barrier. Furthermore, the smaller ΔE signifies the lower degree of polarization for ZnS/ZnSe, which is beneficial to suppress side reactions and achieve structural stability. Moreover, the discharge plateau of the ZnS/ZnSe electrode is higher than that of the ZnS and ZnSe electrodes in Supporting Information: Figure S8, which illustrates elevated sodium intercalation potentials induced by the heterostructure. The elevated discharge

plateau effectively suppresses dendrite formation and accommodates volumetric changes, thereby significantly enhancing cycling stability. The sodium storage performance of ZnS, ZnS/ZnSe, and ZnSe electrodes was compared, including specific capacity, rate capacity, and cycling stability, and was further evaluated in half-cells. As shown in Figure 3C, the ZnS/ZnSe electrode exhibits markedly superior rate capacity relative to the ZnS and ZnSe electrodes across different current densities from 0.1 to 20 A g^{-1}. Specifically, the discharge specific capacities of ZnS/ZnSe electrode were 796, 795, 773, 756, 747, 743, 737, and 727 mAh g^{-1} at 0.1, 0.2, 0.5, 0.8, 1, 2, 5, and 10 A g^{-1}. ZnS/ZnSe electrode maintains a high capacity of 710 mAh g^{-1} even at an ultrahigh current density of 20 A g^{-1}. Upon reverting the current density to 0.1 A g^{-1}, the ZnS/ZnSe electrode regains a high capacity of 815 mAh g^{-1}, demonstrating excellent reversibility. Furthermore, the capacity retention from 0.1 to 20 A g^{-1} was significantly higher for ZnS/ZnSe (89.3%) than for ZnS (48.3%) and ZnSe (49.7%). In addition, the rate performance of ZnS/ZnSe electrode significantly surpasses that of previously reported ZnS-based and ZnSe-based compounds in Supporting Information: Figure S9A,C, illustrating the pronounced benefits of heterostructure engineering in significantly enhancing rate performance. Figure 3D,E presents the charge/discharge profiles at various current densities and over consecutive cycles. The stable voltage plateaus and high initial coulombic efficiency of 95.2% confirm excellent electrochemical reversibility of the ZnS/ZnSe electrode. The long-term cycling tests were conducted at 10 A g^{-1} after initial activation through two preconditioning cycles at 0.05 A g^{-1} in Figure 3G. The capacity of the ZnS/ZnSe electrode slightly descends before the 50th cycle and increases to 900 mAh g^{-1} after 200 cycles. The ZnS/ZnSe electrode delivers a remarkably stable capacity of 904 mAh g^{-1} with a high capacity retention of 93.2%, while the ZnS electrode maintains a low capacity of 488 mAh g^{-1}. Moreover, the capacities of ZnS and ZnSe electrodes descend before the 100th and 250th cycle and increase to 267 and 423 mAh g^{-1} after 400 cycles and 200 cycles, respectively. The capacity recovery phenomenon observed in ZnS/ZnSe is attributable to a gradual transition storage mechanism from conversion to surface redox pseudocapacitive storage mechanisms, facilitated by structural evolution within the electrode material, as will be systematically analyzed later. To assess the cycling stability at even higher rates, the ZnS/ZnSe electrode was tested at 15 A g^{-1} (Figure 3H). Impressively, ZnS/ZnSe retained a high capacity of 803 mAh g^{-1} over 1800 cycles, achieved a capacity retention of 89.0% and minimal average capacity decay of only 0.05 mAh g^{-1} per cycle. As demonstrated in Supporting Information: Figure S9B,D, the cycling performance of the ZnS/ZnSe electrode markedly surpasses those of previously reported ZnS- and ZnSe-based electrodes, illustrating the effectiveness of constructing heterojunctions in maintaining superior structural stability. Figure 3F presents the remarkable consistency of voltage-time profiles recorded from the 1000th to 1005th cycles at 15 A g^{-1}, where each cycle is completed within 221 s, directly evidencing the outstanding electrochemical reversibility under extreme fast-charging scenarios.

The exceptional rate performance and long-term cycling performance demonstrated by ZnS/ZnSe electrode notably surpass the theoretical capacity of ZnS (550 mAh g^{-1}) and ZnSe (371 mAh g^{-1}), based on the typical conversion reaction. To elucidate the underlying reasons for this enhanced capacity, the Na^+ storage mechanisms were thoroughly investigated using cyclic voltammetry (CV) at a scan rate of 2 mV s^{-1} over the initial 100 cycles. In Figure 4A, the CV curves of ZnS from the 2nd to the 20th cycle show a gradual intensification of both oxidation peak 1 and reduction peak 2, which correspond to the conversion reaction ($ZnS + 2Na^+ + 2e^- \leftrightarrow Zn + Na_2S$). However, subsequent cycles show stable oxidation peak intensity after 100 cycles, whereas the reduction peak progressively diminishes and eventually vanishes (Figure 4B,C). The results illustrate that the ZnS particles undergo an initial increase in active site exposure and reaction kinetics due to the conversion reaction during the first few cycles, followed by diminishing conversion efficiency due to the thickening of the solid-electrolyte interphase (SEI) layer. In contrast to ZnS, both ZnSe and ZnSe/ZnS exhibit stronger redox peaks and then gradually weaken (Figure 4E,I), indicating their higher electrochemical reactivity compared to ZnS. During prolonged cycling, Peak1 and Peak2 in ZnSe and ZnS/ZnSe gradually weaken, while new peaks (Peak2, 3, 5, and 6) emerge and intensify over successive cycles (Figure 4F,J,). These evolving redox peaks are more explicitly illustrated from the 2nd to 100th cycle in Figure 4G,K. According to previous reports [46, 47], the emerging peaks are associated with surface redox pseudocapacitive reaction. Compared with ZnSe, the ZnS/ZnSe heterostructure demonstrates significantly intensified redox peaks relative to ZnSe, suggesting superior pseudocapacitive charge storage capabilities originating from porous structure and stronger conductivity. The discharge–charge curves of ZnS/ZnSe corresponding to CV curves are presented in Figure 4M,N. The ZnS/ZnSe shows a pair of discharge-charge plateaus from 2nd to 20th cycles, while subsequently developing three distinct charge plateaus during later cycles (81st to 100th cycles), consistent with the evolution observed in CV analysis. Furthermore, Figure 4N presents three distinct charge plateaus from 81st to 100th cycles, which correspond to the Peak1, Peak2, and Peak3. The emergence of these new peaks indicates the conversion reaction toward pseudocapacitive charge storage, which plays a key role in enhancing the specific capacity. However, the discharge–charge plateaus of ZnS and ZnSe display considerably less distinct discharge–charge plateaus (Supporting Information: Figure S11A,B), confirming that heterostructure engineering significantly enhances the prominence of the surface redox reactions. To quantitatively assess capacity contributions, CV curves of the ZnS/ZnSe at varying scan rates were analyzed (Figure 4O). The fitting *b*-values of peak1 and peak4 are close to 0.5, suggesting diffusion-controlled processes, while values for other peaks approach 1, illustrating predominantly surface-controlled pseudocapacitive processes. By fitting these results with the Equation $i(v) = k_1 v + k_2 v^{1/2}$, the capacitance contribution ($k_1 v$) for the ZnS/ZnSe is significantly higher than that of ZnS and ZnSe [48, 49]. This result suggests that an engineered heterostructure substantially benefits surface redox pseudocapacitance originating from porous structure and the built-in electric field effect. Ultimately, these enhancements result in the observed capacity significantly surpassing theoretical values, predominantly driven by surface-dominated pseudocapacitive charge storage mechanisms.

To verify the transformation of the Na^+ storage mechanism from conversion reaction to surface redox pseudocapacitive

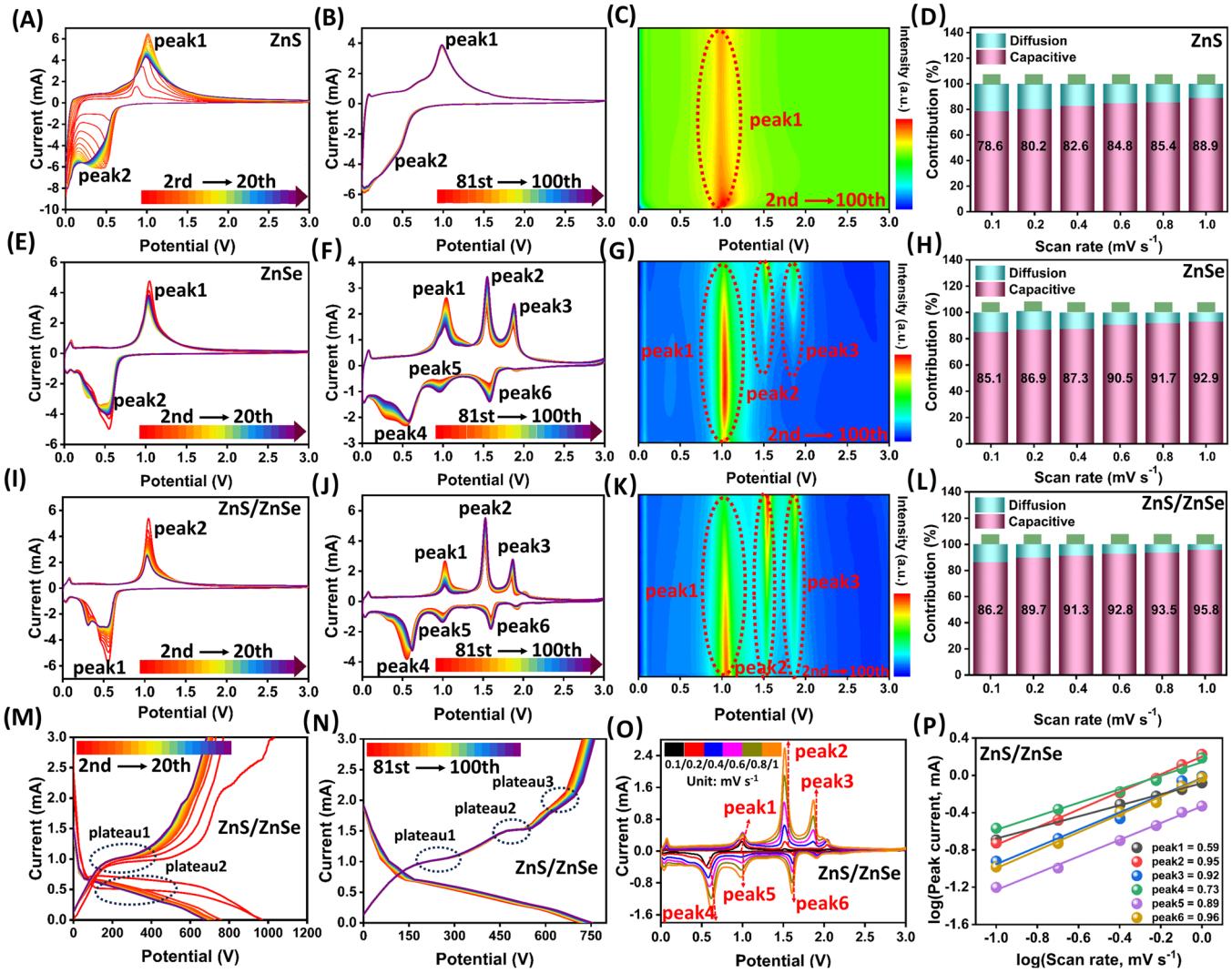

FIGURE 4 | Cyclic voltammetry (CV) curves at 2 mV s^{-1} and corresponding to counter plots of ZnS (A–C), ZnSe (E–G), and ZnS/ZnSe (I–K) from the 2nd to 100th cycle. Discharge-charge curves of ZnS/ZnSe (M–N) from the 2nd to 100th cycle. CV curves at different scan rates of ZnS/ZnSe (O), *b*-values for different redox peaks (P), and the capacitive contributions of ZnS/ZnSe (D), ZnSe (H), and ZnS (L).

reaction, in situ XRD measurements were performed during the initial two charge–discharge cycles and the 300th and 301st cycles (Figure 5A,B). Over the initial discharge process, the diffraction peaks at 2θ of 28.1°, 45.5°, and 53.8° are attributed to the (111), (220), and (311) planes of ZnSe (PDF#37-1463), while the diffraction peaks at 28.1° and 47.8° are corresponds to the (111) and (220) planes of ZnS (PDF#05-0566) [35, 36]. As the voltage decreased to approximately 0.41 V, these characteristic peaks of ZnS and ZnSe accordingly disappear, illustrating that ZnS and ZnSe have been fully transformed into Zn, Na_2S, and Na_2Se. Meanwhile, two new diffraction peaks emerging at approximately 22.5° and 38.5° can be attributed to the formation of Na_2Se (PDF#23-0527) and Na_2S (PDF#23-0441), resulting from the conversion reaction between Na^+ and ZnS/ZnSe, align with the XRD evolution trend shown in Supporting Information: Figure S12A. However, Zn diffraction peaks were not observed in the in situ XRD pattern in the initial discharge, likely due to their low content and crystallinity. As the electrode is recharged between 0.84 and 1.0 V, the diffraction peaks of the Na_2Se and Na_2S gradually disappear, demonstrating their reconverted into ZnSe and ZnS. To further elucidate the evolution of the Na^+ storage mechanism, the electrode after 299 cycles was re-examined by in situ XRD (Figure 5B). Two new diffraction peaks appear at approximately 43.6° and 54.5° can be assigned to (101) and (102) planes of Zn, while the diffraction peaks of Na_2S, Na_2Se, and ZnSe can still be probed. In contrast to the initial in situ observations, the diffraction peaks of ZnS/ZnSe persist throughout the entire charge–discharge process during the 300th and 301st cycles. These observations clearly verify a transition of the Na^+ storage mechanism toward surface redox pseudocapacitive reaction.

CV tests were performed between the 300th and 315th cycles and shown in Figure 5C. The excellent reproducibility of CV profiles suggests highly reversible redox reactions of the ZnS/ZnSe electrode. Notably, in contrast to earlier CV profiles (Figure 4K), the peak belonging to the conversion reaction has completely disappeared in Figure 5D, while the peaks associated with the surface redox pseudocapacitive reaction are significantly enhanced in Figure 6D,E. According to the above results, the Na^+ storage mechanism has changed from a conversion reaction to a surface redox pseudocapacitive reaction after extensive cycling. Moreover, the differential capacity (d*Q*/

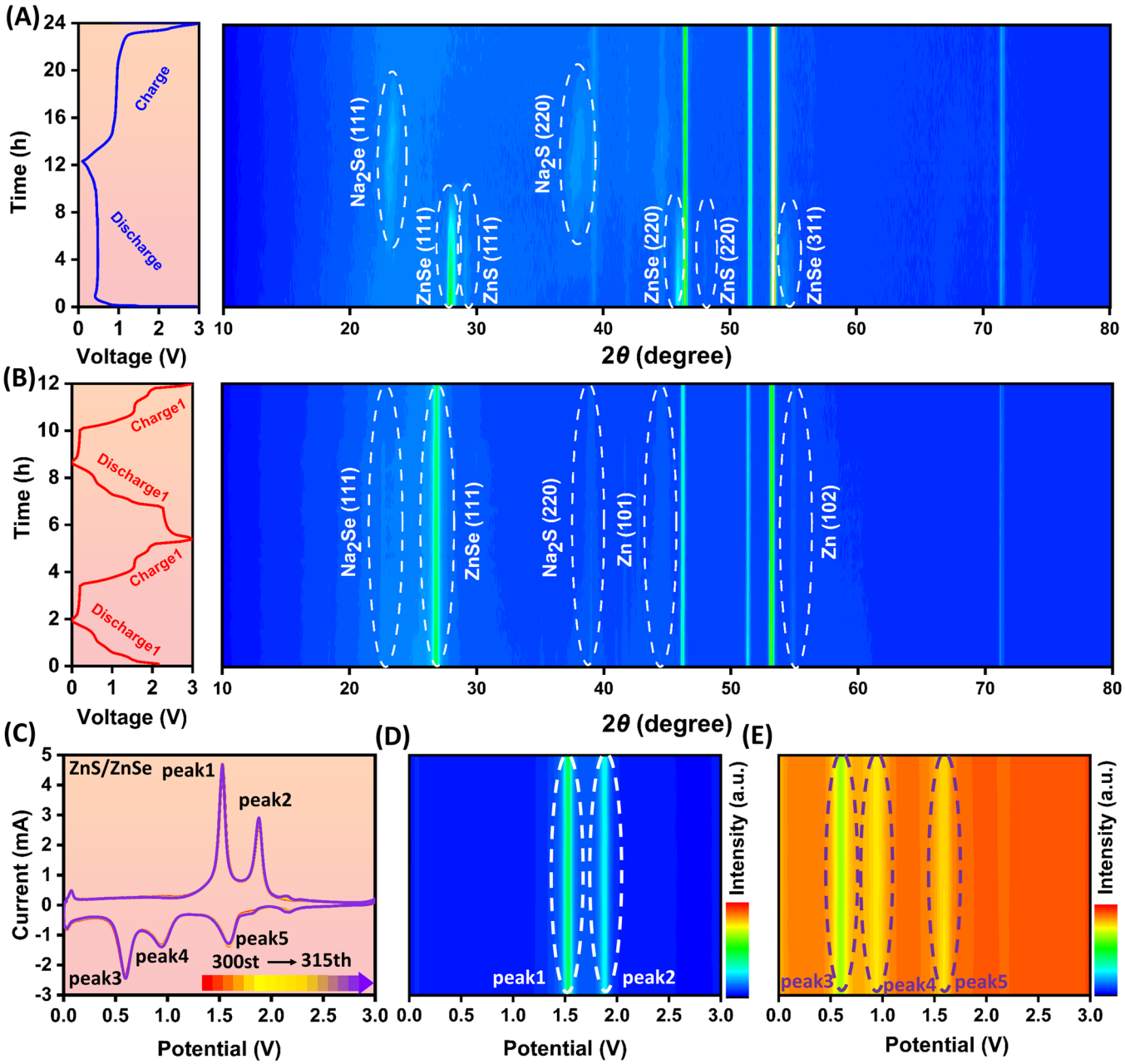

FIGURE 5 | Contour plots of ZnS/ZnSe in the initial cycle (A), 300th and 301st (B). Cyclic voltammetry (CV) curves of ZnS/ZnSe from 300th to 315th cycles (C) and corresponding to the contour plots of oxidation peaks (D) and reduction peaks (E).

d*V*) curves in Supporting Information: Figure S12C,D reveal that the capacitance contribution primarily stems from surface redox pseudocapacitive behavior [50, 51]. Consequently, the substantially enhanced Na^+ storage capacity for the ZnS/ZnSe heterostructure compared to ZnS and ZnSe demonstrates that rationally designed heterostructures effectively enhance surface redox pseudocapacitive reactions, enabling high-capacity and ultrafast-charging SIBs.

To analyze the reaction kinetics of ZnS, ZnS/ZnSe, and ZnSe during the conversion reaction, GITT profiles were acquired by applying a 4800-second current pulse at 0.1 A g^{-1} after two cycles. Figure 6A–C present the GITT profiles of ZnS/ZnSe with lower overpotential, suggesting enhanced Na^+ reaction kinetics by the heterostructure. Single-step GITT analysis profiles at 1.5 V (Supporting Information: Figure S13) reveal that the ZnS/ZnSe exhibits significantly smaller ΔEτ and IR drop values compared to both ZnS and ZnSe, corroborating improved ion diffusion kinetics [52, 53]. For quantitative analysis of Na^+ diffusion kinetics, the Na^+ diffusion coefficient was calculated using the equation:

$$D_{Na^+} = \frac{4}{\pi\tau} \left(\frac{mV_m}{MA}\right)^2 \left(\frac{\Delta E_s}{\Delta E_\tau}\right)^2, \quad (1)$$

where m, V_m, A, ΔE_s, and ΔE_τ represent the mass, molar volume, molar mass, area, and transient voltage change under the equilibrium and constant current state. By GITT calculation, the average D_{Na+} of the ZnS/ZnSe was calculated to be 2.60×10^{-12} $cm^2 s^{-1}$, which is higher than those of the ZnS (2.55×10^{-13} $cm^2 s^{-1}$) and ZnSe (4.74×10^{-13} $cm^2 s^{-1}$).

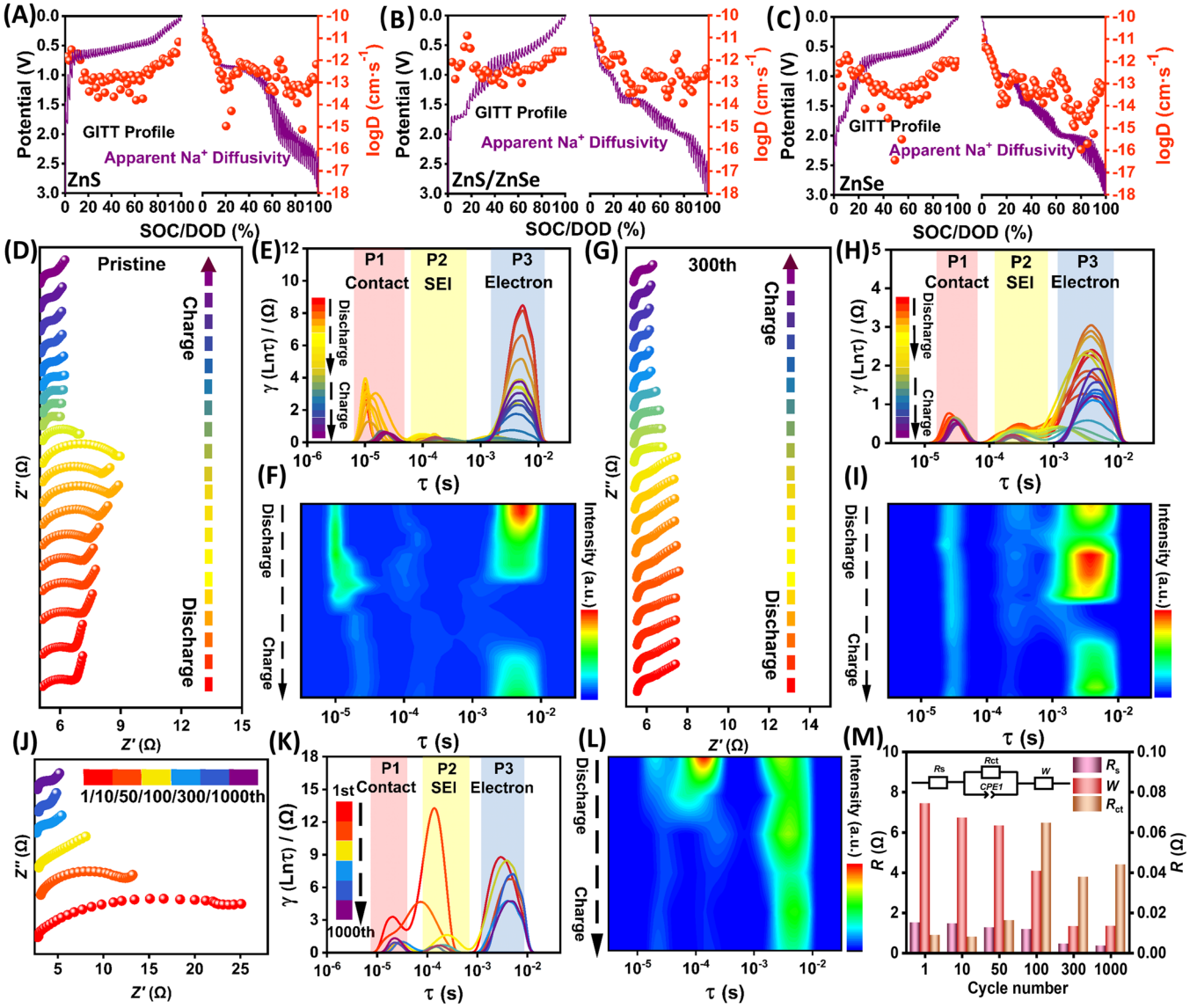

FIGURE 6 | GITT curves with corresponding D_{Na+} (A–C). In situ EIS spectra in the initial cycle of ZnS/ZnSe electrode (D) and corresponding DRT curves and contour map (E, F), in situ EIS spectra in the 300th cycle (G) and corresponding DRT curves and contour map (H, I). Ex situ EIS plots of the ZnS/ZnSe electrode at different cycles (J) and corresponding DRT curves and contour map (K, L), the calculated R_s, R_{ct}, and W values (M). DRT, distribution of relaxation times.

The enhanced D_{Na+} value illustrates that the ZnS/ZnSe heterostructure promotes Na^+ diffusion through the built-in electric field, creating favorable conditions for conversion reaction into surface redox pseudocapacitive reactions. Moreover, in situ EIS was employed to dynamically monitor the charge-transfer kinetics and interfacial evolution of ZnS/ZnSe during the conversion process (Figure 6D and Supporting Information: Figure S14A,D). The evolution of interfacial resistances was quantitatively analyzed through distribution of relaxation times (DRT), a model-free method that enables clear separation of concurrent electrochemical processes [54, 55]. As shown in Figure 6E, the DRT analysis identified three characteristics timescales: the fastest process (P1, $\tau = 10^{-5} - 10^{-4}$ s) originates from the contact resistance involving active materials and current collector, while the moderate process (P2, $\tau = 10^{-4} - 10^{-3}$ s) represents solid electrolyte interphase resistance (R_{SEI}) on surface of the electrode, and the lowest process (P3, $\tau = 10^{-3}$–10^{-2} s) corresponds to the charge transfer resistance (R_{ct}). In the pristine ZnS/ZnSe electrode, the shift of the relaxation time constant τ toward the lower frequency region (P1) indicates that the active material particles have lost good electrical contact with the current collector, leading to an increase in contact resistance. Furthermore, the intensity of the P3 peak responding to the R_{ct} initially drops rapidly from 8.5 to 2.5 Ω and then rebounds to higher values (3.8 Ω). These results evolution suggest that the electrode undergoes a structure change due to the insertion of Na^+ based on the conversion reaction. In addition, ZnS and ZnSe electrodes exhibit a similar overall trend of P3 peak (Supporting Information: Figure S14B,C), although their DRT curves (Supporting Information: Figure S14) show higher peak intensities and lower overlap of P1 and P2 peaks compared to the ZnS/ZnSe electrode. These results suggest that the heterostructure construction can improve conductivity and enhance Na^+ diffusion kinetics. The in situ EIS spectra of ZnS/ZnSe were collected to study reaction kinetics based on the surface redox

pseudocapacitive reactions after 300 cycles (Figure 6H). The peak intensities exhibit stable fluctuations within a narrow amplitude range, demonstrating the electrode's stable electrochemical state (Figure 6I). Compared with pristine ZnS/ZnSe, the cycles ZnS/ZnSe electrode shows markedly reduced contact resistance and SEI resistance, and charge transfer resistance, confirming a remarkable enhancement in reaction kinetics associated with the transition to pseudocapacitive mechanisms facilitated by internal heterointerface and optimized ion transport pathways. Subsequently, ex situ EIS test for ZnS/ZnSe electrode at various cycles reveals significant variations in both intensity and position of the P1 and P2 peaks (Figure 6K,L), showing a continuous decline in the first 100 cycles and maintaining consistently low impedance values after 300 cycles. This behavior reflects a structural optimization process resulting in stabilized and accelerated reaction kinetics. Figure 6M presents the evolution of interfacial contact resistance (R_s), charge transfer resistance (R_{ct}), and Warburg impedance (W) of Na^+ in the electrode derived from equivalent circuit fitting [56, 57]. In contrast with the initial and stabilized impedance values, the ZnS/ZnSe electrode shows ultrafast reaction kinetics after 300 cycles, consistent with in situ analyses. Moreover, these comprehensive GITT and in situ/ex situ studies provide compelling evidence supporting the transition of Na^+ storage mechanism from conventional conversion reaction to surface redox pseudocapacitive reaction, driven by kinetic

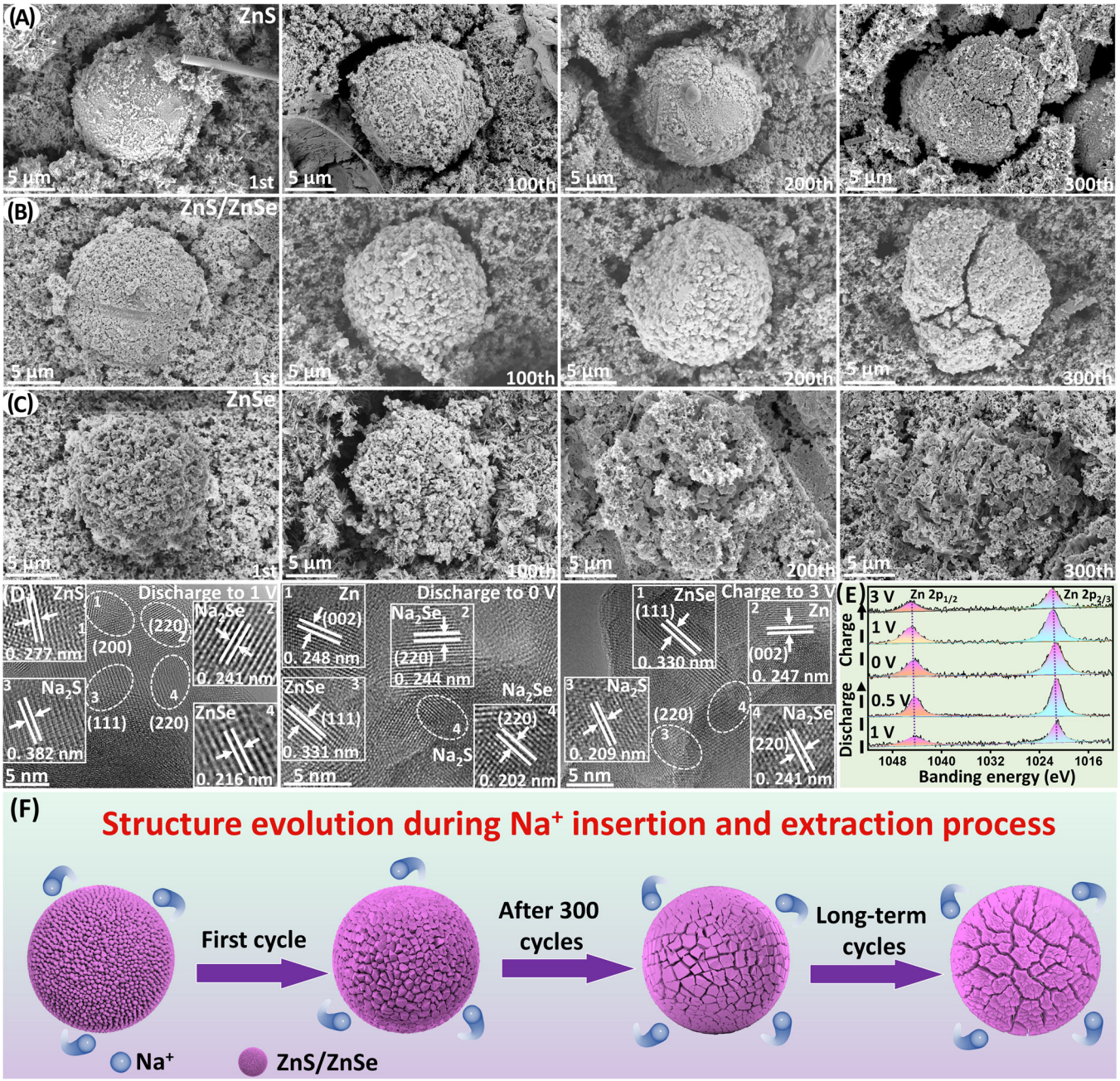

FIGURE 7 | Ex situ SEM of ZnS (A), ZnS/ZnSe (B), and ZnSe (C). Ex situ HRTEM of ZnS/ZnSe (D) after 300 cycles. Ex situ high-resolution XPS spectra of the ZnS/ZnSe (E) after 300 cycles. Schematic diagram of morphological evolution of the ZnS/ZnSe (F). HRTEM, high-resolution transmission electron microscopy; SEM, scanning electron microscopy; XPS, X-ray photoelectron spectra.

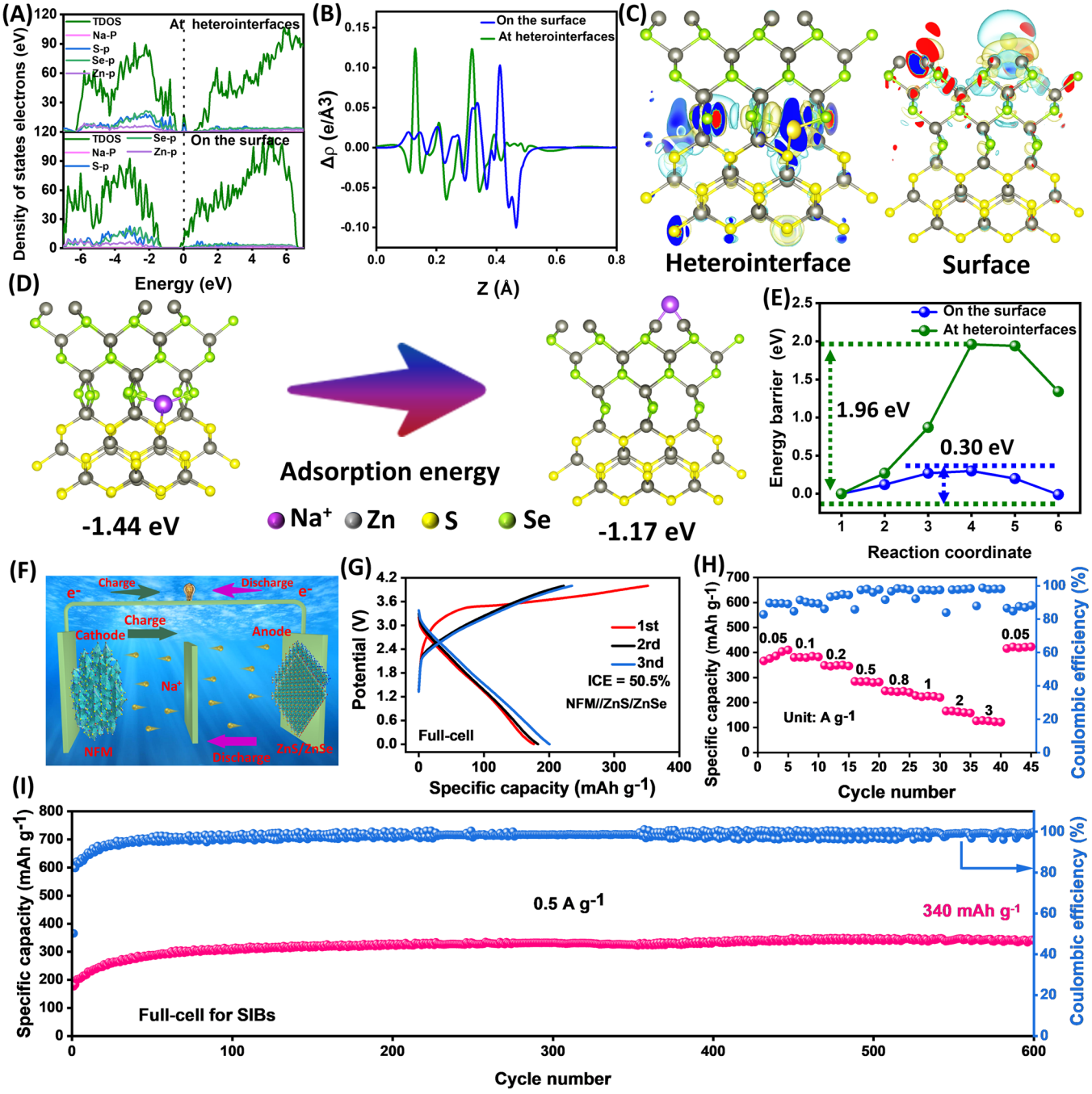

FIGURE 8 | Theoretical computation of total density of states (TDOS) (A). The planar-averaged electron density difference Δρ (B), side view of the charge density difference of ZnS/ZnSe at heterointerfaces and on the surface (C), where the yellow and blue regions denote the gain and loss of electrons. Adsorption energy of Na atom at heterointerfaces and on the surface (D). The migration energy barriers (E). Schematic illustration of the NFM//ZnS/ZnSe system (F). Charge–discharge profiles of the NFM//ZnS/ZnSe full-cell (G), rate (H), and long-term cycling performance (I) of the NFM//ZnS/ZnSe full-cell.

enhancements arising from heterointerface formation and structural evolution.

The morphological evolution of ZnS/ZnSe was systematically investigated through ex situ SEM and TEM analyses. As presented in Figure 7A,B, the ZnS and ZnS/ZnSe retain their original architecture without obvious degradation after continuous discharge/charge process up to 200 cycles, while the ZnSe exhibits significant volume expansion within the same cycling period (Figure 7C). This phenomenon can be primarily attributed to the inherently poor electrical conductivity of ZnS, limiting its redox reactivity during cycling and consequently minimizing volume strain. Importantly, the ZnS/ZnSe heterostructure not only retains the structural stability of ZnS but also utilizes its heterointerface and porous architecture to effectively absorb mechanical stress and mitigate volume expansion. However, upon cycling to 300 cycles, both ZnS and ZnS/ZnSe show visible cracks, while ZnSe experiences severe structural collapse due to its higher electrochemical reactivity and lower bond energy. This structural collapse directly corresponds to the abrupt capacity decay observed in the ZnSe electrode upon

reaching about 550 cycles (Figure 3G). To further elucidate the sodium storage mechanism of the ZnS/ZnSe, *ex situ* HRTEM characterization was performed and depicted in Figure 7D. When discharged to 1.0 V, HRTEM analysis reveals well-defined lattice fringes of 0.277, 0.216, 0.382, and 0.241 nm, which correspond to the (200), (220), (111), and (220) planes of ZnS, ZnSe, Na_2S, and Na_2Se, respectively. Moreover, the lattice fringe of 0.248 nm indexing to the (002) plane of metallic Zn was probed when discharged to 0 V, which originates from the conversion reaction between ZnS/ZnSe and Na^+. However, when the samples were charged to 3 V (Figure 7D), the lattice fringes of ZnS, ZnSe, metallic Zn, Na_2S, and Na_2Se were still observable, implying incomplete or suppressed conversion reactions during the charging phase. The crystal planes observed in the aforementioned TEM analysis can also be identified in the XRD patterns. From the 1st cycle to the 300th cycle, it can be observed that the peak intensity of the (111) plane of ZnS/ZnSe gradually broadens and weakens, along with a shift to lower angles (Supporting Information: Figure S15B). These observations indicate that the transition from the conversion reaction to the surface redox pseudocapacitive reaction is accompanied by an increase in the interplanar spacing and a decrease in the crystallinity of ZnS/ZnSe. Ex situ high-resolution XPS spectra (Figure 7E) further substantiate this interpretation, showing consistent positions of Zn $2p_{1/2}$ and Zn $2p_{2/3}$ peaks. These results strongly support a shift from bulk conversion reactions toward surface redox pseudocapacitive behavior. Moreover, Figure 7F schematically illustrates the morphological and mechanistic evolution of ZnS/ZnSe electrodes throughout cycling. Initially, the ZnS/ZnSe electrode experiences a conversion reaction accompanied by substantial volume change. After prolonged cycling (~300 cycles), the reaction mechanism shifts to surface redox pseudocapacitive reaction, facilitated by the abundant heterointerface and optimized Na^+ diffusion pathway within the heterostructure.

To further elucidate the mechanistic transition from conversion reaction to surface redox pseudocapacitive reaction, density functional theory (DFT) calculations were employed to study the total density of states (TDOS), electron density difference Δρ, adsorption energy, and migration energy barriers within the ZnS/ZnSe heterostructure. Two structural models were constructed to represent Na atom reaction sites: one for conversion reactions occurring at heterointerfaces (Supporting Information: Figure S16C) and another for surface redox pseudocapacitive reactions (Supporting Information: Figure S16D) [23, 58]. The density of states of two structural models suggests that the ZnS/ZnSe heterostructure possesses obvious semiconductor characteristics. Compared with the TDOS, the Na-interaction model at heterointerfaces shows higher conductivity compared to the surface-interaction model, attributable to the built-in electric field formed at the heterointerfaces. Moreover, the charge density difference analyses clearly indicated more substantial charge accumulation (yellow) and depletion (blue) at heterointerfaces relate to surface sites (Figure 8B,C). The result demonstrates that redox reactions at the heterointerfaces are significantly pronounced than those at the surface. The Na adsorption models displayed in Figure 8D (side-view representations) further illustrated distinct adsorption energies. Specifically, the calculated adsorption energy at heterointerfaces (−1.44 eV) indicates a stronger binding affinity for Na atoms compared to surface adsorption sites (−1.18 eV). The resultant weaker surface binding facilitates faster Na^+ diffusion kinetics on surfaces compared to heterointerfaces, implying a potential redox pseudocapacitive reaction occurring on the surface. To quantify these kinetic differences, structural models of Na^+ migration pathways at both heterointerfaces and surface regions were systematically evaluated (Supporting Information: Figure S17). Corresponding energy barriers (Figure 8E) demonstrated significantly lower Na^+ diffusion barrier on the ZnS/ZnSe surface (0.30 eV) compared to heterointerfaces (1.96 eV), suggesting predominant surface diffusion rather than bulk diffusion. These computational findings provide compelling theoretical evidence of the experimentally observed mechanistic transition, indicating that prolonged cycling promotes a shift in the dominant Na^+ storage mechanism from conversion reaction to surface redox pseudocapacitive behavior.

The exceptional cycling stability and rate capability demonstrated by ZnS/ZnSe porous microspheres in half-cell configurations prompted further investigation of their practical application in full-cell SIBs. Accordingly, a full-cell was assembled by pairing ZnS/ZnSe anode with $NaNi_{1/3}Fe_{1/3}Mn_{1/3}O_2$ (NFM) cathode, the detailed structure of which is presented in Supporting Information: Figure S18. The operational mechanism of the constructed NFM//ZnS/ZnSe full-cell is schematically illustrated in Figure 8F. Figure 8G shows the charge-discharge profiles of the full-cell, highlighting a distinct voltage plateau around 3.50 V at 0.5 A g^{-1}. The assembled full-cell exhibits initial charge and discharge capacities of 352 and 177 mAh g^{-1} based on the active materials for the anode, respectively, corresponding to an initial Coulombic efficiency (ICE) of 50.2%. Subsequent evaluation of the rate capability demonstrates that the NFM//ZnS/ZnSe achieves average discharge capacities of 389, 382, 347, 283, 244, 224, 163, 125 mAh g^{-1} at 0.05, 0.1, 0.2, 0.5, 0.8, 1, 2, and 3 A g^{-1}, respectively. Remarkably, upon returning to a lower current density of 0.05 A g^{-1}, the cell exhibits a fully reversible capacity of 420 mAh g^{-1}, demonstrating exceptional electrochemical reversibility. Notably, the full-cell demonstrates exceptional rate capability, surpassing the performance of the most previously reported ZnS-based and ZnSe-based full-cells, as summarized in Supporting Information: Figure S19A. Furthermore, outstanding long-term cycling stability is demonstrated by maintaining a high reversible capacity of 340 mAh g^{-1} after 600 cycles at 0.5 A g^{-1} (Figure 8I), surpassing the performance of many previously reported full-cells for SIBs (Supporting Information: Figure S19B). The practical viability of the NFM//ZnS/ZnSe full-cell is further demonstrated by successfully powering an LED panel using a coin-cell configuration (Supporting Information: Figure S20). These results clearly demonstrate the ZnS/ZnS heterostructure as a highly promising anode material for practical SIBs applications.

3 | Conclusion

In conclusion, this study introduces a facile yet robust synthetic strategy involving hydrothermal growth followed by controlled selenization to fabricate ZnS/ZnSe heterostructure anode via in situ phase transformation. The synergistic combination of abundant heterointerfaces and a porous structure significantly enhances Na^+ diffusion kinetics and effectively alleviates

mechanical stress during repeated cycles. By employing systematic in situ characterization methods and DFT calculations, we elucidated a clear mechanistic transition from conversion reaction to surface redox pseudocapacitive reaction. As a result, the ZnS/ZnSe electrode delivers an extremely remarkable cycling stability, delivering a stable capacity of 803 mAh g^{-1} at 15 A g^{-1} after 1800 cycles, alongside exceptional rate capacity, maintaining 710 mAh g^{-1} even at 20 A g^{-1}. Moreover, the practical applicability of the developed anode was confirmed through assembling an NFM//ZnS/ZnSe full-cell, which showed outstanding long-term cycling performance of 340 mAh g^{-1} at 0.5 A g^{-1} over 600 cycles. This study provides a comprehensive method, integrating rational structural design with in-depth mechanistic understanding, offering new insights into developing fast-charging anode materials for SIBs.

Acknowledgments

This study was supported by the Guangxi Natural Science Foundation (Grant No. 2024GXNSFAA010515), National Natural Science Foundation of China (Grant nos. No. 51964013W2441017, 22409103), and the "Innovation Yongjiang 2035" Key R&D Program (Grant nos. 2024Z040, 2025Z063).

Conflicts of Interest

The authors declare no conflicts of interest.

References

1. Y. Zhou, Y. Wang, Y. Zhang, et al., "Abundant $Cu_3P/Co_2P/CoP$@NC Heterostructures Boost Charge Transfer Toward Fast and Durable Sodium Storage," *Carbon Energy* 7, no. 6 (2025): e721.

2. F. Cheng, J. Hu, W. Zhang, et al., "Reviving Ether-Based Electrolytes for Sodium-Ion Batteries," *Energy & Environmental Science* 18, no. 14 (2025): 6874–6898.

3. J. Peng, W. Zhang, Q. Liu, et al., "Prussian Blue Analogues for Sodium-Ion Batteries: Past, Present, and Future," *Advanced Materials* 34, no. 15 (2022): 2108384.

4. T. Zhao, L. Wang, C. Zhang, et al., "Comprehensive Insights into Sodium Storage in Pitch-Derived Porous Hard Carbon," *Carbon Energy* 7, no. 7 (2025): e649.

5. P. Hong, C. Xu, C. Yan, Y. Dong, H. Zhao, and Y. Lei, "Prussian Blue and Its Analogues for Commercializing Fast-Charging Sodium/Potassium-Ion Batteries," *ACS Energy Letters* 10, no. 2 (2025): 750–778.

6. G. Zhang, H. Gao, D. Zhang, et al., "Transformative Catalytic Carbon Conversion Enabling Superior Graphitization and Nanopore Engineering In Hard Carbon Anodes for Sodium-Ion Batteries," *Carbon Energy* 7, no. 6 (2025): e713.

7. T. Park, J. Kim, Y. Jung, J. Sun, and K. Min, "Design Strategies for Fast-Charging Multiphase Na-Ion Layered Cathodes: Dopant Selection via Computational High-Throughput Screening," *Journal of Energy Chemistry* 107 (2025): 103–113.

8. H. Zhang, Y. Gao, J. Peng, et al., "Prussian Blue Analogues With Optimized Crystal Plane Orientation and Low Crystal Defects Toward 450 Whkg," *Angewandte Chemie-International Edition* 62 (2023): e202303953.

9. P. Yu, W. Tang, F. F. Wu, et al., "Recent Progress In Plant-Derived Hard Carbon Anode Materials for Sodium-Ion Batteries: A Review," *Rare Metals* 39, no. 9 (2020): 1019–1033.

10. J. K. Li, K. Z. Wang, J. Hu, et al., "In-situ reconstruction of N-doped carbon nanoflower coating layer for enhancing high pseudo-capacitance in Bi-based fast-charging lithium-ion batteries," *Rare Metals* 44, no. 3 (2025): 1617–1631.

11. M. Park, M. Park, et al., "Carbon Nanofiber Decorated Ternary Transition Metal Oxide Anodes for Fast Charging Lithium-Ion Batteries," *Energy Technology* 11, no. 11 (2022): 2200293.

12. Y. Liu, Y. Zhu, and Y. Cui, "Challenges and Opportunities Towards Fast-Charging Battery Materials," *Nature Energy* 4, no. 7 (2019): 540–550.

13. B. Peng, S. Xu, Z. Lv, et al., "Toward Extremely Fast Charging Through Boosting Intercalative Redox Pseudocapacitance: A $SbCrSe_3$ Anode for Large and Fast Sodium Storage," *Advanced Energy Materials* 13, no. 2 (2023): 202203187.

14. B. Wu, S. Niu, C. Wang, et al., "Amorphous Vanadium Oxide Nanosheets With Alterable Polyhedron Configuration for Fast-Charging Lithium-Ion Batteries," *Small* 19, no. 43 (2023): 2303360.

15. S. Vishwanathan, M. K. Mohanta, P. Jena, and H. S. S. R. Matte, "Experimental and Theoretical Insights on Interface Engineered FeS/rGO as Anode for Fast-Charging Lithium- and Sodium-Ion Batteries," *Small* 21, no. 17 (2025): 2410482.

16. C. Xu, J. Yang, K. Chen, et al., "$CoSe_2$-Modified Multidimensional Porous Carbon Frameworks as High-Performance Anode for Fast-Charging Sodium-Ion Batteries," *Chemical Engineering Journal* 497 (2024): 154875.

17. Y. Zhang, B. Han, S. Tan, et al., "Interfacial Engineering of Metal Chalcogenides-Based Heterostructures for Advanced Sodium-Ion Batteries," *Advanced Energy Materials* 15, no. 15 (2025): 202404796.

18. T. Li, B. Wang, H. Song, et al., "Deciphering the Performance Enhancement, Cell Failure Mechanism, and Amelioration Strategy of Sodium Storage In Metal Chalcogenides-Based Anodes," *Advanced Materials* 36, no. 25 (2024): 2314271.

19. Z. Hao, X. Shi, Z. Yang, L. Li, and S.-L. Chou, "Developing High-Performance Metal Selenides for Sodium-Ion Batteries," *Advanced Functional Materials* 32, no. 51 (2022): 2208093.

20. Y. Zhang, Q. Zhou, J. Zhu, Q. Yan, S. X. Dou, and W. Sun, "Nanostructured Metal Chalcogenides for Energy Storage and Electrocatalysis," *Advanced Functional Materials* 27, no. 35 (2017): 1702317.

21. Y. Gong, Y. Li, Y. Li, M. Liu, Y. Bai, and C. Wu, "Metal Selenides Anode Materials for Sodium Ion Batteries Synthesis, Modification, and Application," *Small* 19, no. 4 (2023): 202206194.

22. Q. Huang, T. Xie, Y. Luo, et al., "A Comprehensive Review on Zinc-Based MOFs and Their Derivatives for Alkali-Ion Batteries: Synthesis, Applications, and Future Prospects," *Advanced Functional Materials* 35 (2025): 2508749.

23. Z. Khanam, L. Luo, M. Mushtaq, et al., "Robust Pseudocapacitive Na^+ Intercalation Induced by MoS_2 on Active Mo_2C Current Collector Interface for High Areal Capacity Sodium-Ion Batteries," *Nano Energy* 125 (2024): 109590.

24. Y. Gao, P. Hai, L. Liu, et al., "Balanced Crystallinity and Nanostructure for SnS_2 Nanosheets Through Optimized Calcination Temperature Toward Enhanced Pseudocapacitive Na^+ Storage," *ACS Nano* 16 (2022): 14745–14753.

25. D. Tang, R. Yu, Y. Jiang, et al., "Electrochemically In Situ Formed Rocksalt Phase In Titanium Dioxide Determines Pseudocapacitive Sodium-Ion Storage," *Nature Communications* 16, no. 1 (2025): 2015.

26. X. Hu, P. Ma, Z. Sun, et al., "Ultrafast Na^+ Diffusion Enabled by Defective 3D In_2S_3/MXene Nanostructure Toward High-Rate Sodium Ion Batteries," *Advanced Energy Materials* 15, no. 29 (2025): 2500443.

27. C. Liu, B. Wang, Z. Song, et al., "Enabling Electron Delocalization by Conductor Heterostructure for Highly Reversible Sodium Storage," *Advanced Functional Materials* 34, no. 14 (2024): 2312905.

28. Y. Zhang, J. Guo, X. Liu, et al., "Heterostructure Interface Construction of Zinc/Cobalt Sulfides Derived From Binary Metal-Organic Framework Toward Ultrastable Sodium-Ion Half/Full Batteries," *Advanced Functional Materials* 35 (2025): 2504553.

29. Y. Jiang, F. Wu, Z. Ye, et al., "Confining $CoTe_2$-ZnTe Heterostructures on Petal-Like Nitrogen-Doped Carbon for Fast and Robust Sodium Storage," *Chemical Engineering Journal* 451 (2022): 138430.

30. L. Han, J. Luo, R. Zhang, et al., "Arrayed Heterostructures of MoS_2 Nanosheets Anchored TiN Nanowires as Efficient Pseudocapacitive Anodes for Fiber-Shaped Ammonium-Ion Asymmetric Supercapacitors," *ACS Nano* 16, no. 9 (2022): 14951–14962.

31. H. Zhang, F. Yuan, S. Xue, et al., "Constructing ZnS@Hard Carbon Nanosheets for High-Performance and Long-Cycle Sodium-Ion Batteries," *Chemical Engineering Journal* 509 (2025): 161551.

32. T. Hou, B. Liu, X. Sun, et al., "Covalent Coupling-Stabilized Transition-Metal Sulfide/Carbon Nanotube Composites for Lithium/Sodium-Ion Batteries," *ACS Nano* 15, no. 4 (2021): 6735–6746.

33. M. Zhang, S. Wang, J. Zhu, et al., "Optimized Heterostructures by Preferred Crystal Orientation for Ultrafast Sodium Storage," *Advanced Functional Materials* 35, no. 29 (2025): 2500165.

34. M. Sharma, R. Gulati, and R. S. Dhaka, "Synergistic Role of Transition Metals and Polyanionic Frameworks in Phosphate-Based Cathode Materials for Sodium-Ion Batteries," *Coordination Chemistry Reviews* 543 (2025): 216912.

35. Y. Jin, H. Seong, J. H. Moon, et al., "Study on Colloidal Synthesis of ZnS Nanospheres Embedded in Reduced Graphene Oxide Materials for Sodium-Ion Batteries and Energy Storage Mechanism," *Journal of Alloys and Compounds* 943 (2023): 169076.

36. P. Zhou, L. Wang, M. Zhang, et al., "Hierarchical Structural Modulation and Co-Construction of Selenium Vacancy in ZnSe/$NiSe_2$ Heterojunctions to Enhance Cycling Stability and Fast Ion Diffusion Kinetics for Lithium-Ion and Sodium-Ion Batteries," *Chemical Engineering Journal* 488 (2024): 150829.

37. T. Shi, Y. Yang, M. Yu, W. Zhang, and X. Ning, "N, S Co-Doped Biomass Hard Carbon/ZnS Composite as the Anode Material for High-Rate Sodium-Ion Batteries," *Journal of Energy Storage* 99 (2024): 113246.

38. C. Dong, H. Shao, Y. Zhou, et al., "Construction of ZnS/Sb_2S_3 Heterojunction as An Ion-Transport Booster Toward High-Performance Sodium Storage," *Advanced Functional Materials* 33, no. 9 (2023): 2211864.

39. Z. Gao, J. Wu, X. Ma, et al., "Free-Standing ZnSe-CoFe@CNT/CNF Heterostructure Nanofibers as An Ultra-Long Lifespan and High-Rate Anode for Flexible Lithium Ion and Sodium Ion Batteries," *Journal of Energy Storage* 103 (2024): 114289.

40. Y. Wan, B. Huang, W. Liu, D. Chao, Y. Wang, and W. Li, "Fast-Charging Anode Materials for Sodium-Ion Batteries," *Advanced Materials* 36, no. 35 (2024): 2404574.

41. H. Liang, L. Liu, N. Wang, et al., "Unusual Mesoporous Titanium Niobium Oxides Realizing Sodium-Ion Batteries Operated At −40°C," *Advanced Materials* 34, no. 28 (2022): 2202873.

42. H. Zhang, Z. Lu, B. Liu, C. Yuan, and Y. Cao, "Metal-Electronegativity-Induced Sulfur-Vacancies and Heterostructures of MnS_{1-x}/ZnS-NC@C With Dual-Carbon Decoration for High-Performance Sodium-Ion Storage," *Composites, Part B: Engineering* 274 (2024): 111267.

43. W. Kang, M. Han, M. Niu, et al., "Synchronous Hetero-Interface and Vacancy Engineering for Construction of Pitaya-Like $CoSe_{1-x}$/C@NC@ZnSe Nanosphere Toward Ultrastable Sodium-Ion Half/Full Batteries," *Advanced Energy Materials* 15, no. 26 (2025): 2500276.

44. Y. Liu, L. Tang, H. Wei, et al., "Enhancement on Structural Stability of Ni-Rich Cathode Materials by In-Situ Fabricating Dual-Modified Layer for Lithium-Ion Batteries," *Nano Energy* 65 (2019): 104043.

45. G. Yang, K. Pan, F. Lai, et al., "Integrated Co-Modification of PO_4^{3-} Polyanion Doping and Li_2TiO_3 Coating for Ni-Rich Layered $Lini_{0.6}Co_{0.2}Mn_{0.2}O_2$ Cathode Material of Lithium-Ion Batteries," *Chemical Engineering Journal* 421 (2021): 129964.

46. Q. Wei, X. Chang, D. Butts, et al., "Surface-Redox Sodium-Ion Storage In Anatase Titanium Oxide," *Nature Communications* 14, no. 1 (1 (2023): 7.

47. D. Yuan, Y. Dou, Y. Tian, D. Adekoya, L. Xu, and S. Zhang, "Robust Pseudocapacitive Sodium Cation Intercalation Induced by Cobalt Vacancies At Atomically Thin $Co_{1-x}Se_2$/Graphene Heterostructure for Sodium-Ion Batteries," *Angewandte Chemie International Edition* 60, no. 34 (2021): 18830–18837.

48. Z. Cao, J. Cui, D. Yu, et al., "Synergistic Engineering of Architecture and Composition In Bimetallic Selenide@Carbon Hybrid Nanotubes for Enhanced Lithium- and Sodium-Ion Batteries," *Advanced Functional Materials* 33, no. 51 (2023): 2306862.

49. Y. Xie, J. Yu, L. Cui, et al., "In situ phase transformation of nanoporous Fe_2O_3 dendrite to Fe_2O_3/FeS_2 polycrystalline texture achieving superior rate capability and ultra-long cycling stability With high capacity," *Small Methods* 9 (2025): 2500282.

50. G. Li, L. Zhang, Z. Xu, et al., "Constructing Internal Coupling Reactions Through Iron Substitution to Facilitate Manganese-Based Mixed-Phosphate Cathode for Sodium-Ion Storage," *Advanced Functional Materials* 35, no. 27 (2025): 2425598.

51. G. Yang, B. Liu, F. Lai, et al., "Low-Temperature Synthesis of Amorphous LiF/Li_3Bo_3 Interfaces With F, B Co-Doped Subsurface for Long-Cycling and High-Rate Ni-Rich Cathodes," *Nano Energy* 140 (2025): 111009.

52. J. Li, Y. He, Y. Dai, et al., "Heterostructure Interface Construction of Cobalt/Molybdenum Selenides Toward Ultra-Stable Sodium-Ion Half/Full Batteries," *Advanced Functional Materials* 34, no. 42 (2024): 2406915.

53. C. Wu, Y. Yang, Y. Zhang, et al., "Industrial-Scale Hard Carbon Designed to Regulate Electrochemical Polarization for Fast Sodium Storage," *Angewandte Chemie International Edition* 63, no. 31 (2024): e202406889.

54. J. Pan, Z. Sun, X. Wu, et al., "Mechanically Robust Bismuth-Embedded Carbon Microspheres for Ultrafast Charging and Ultrastable Sodium-Ion Batteries," *Journal of the American Chemical Society* 147, no. 4 (2025): 3047–3061.

55. Y. Lu, C. Z. Zhao, J. Q. Huang, and Q. Zhang, "The Timescale Identification Decoupling Complicated Kinetic Processes In Lithium Batteries," *Joule* 6, no. 6 (2022): 1172–1198.

56. N. Al-Ansi, A. Salah, Q. A. Drmosh, et al., "Carbonized Polymer Dots for Controlling Construction of MoS_2 Flower-Like Nanospheres to Achieve High-Performance Li/Na Storage Devices," *Small* 19, no. 52 (2023): 2304459.

57. X. Jian, Q. Shen, X. Zhao, et al., "Unveiling the Anionic Redox Chemistry in Phosphate Cathodes for Sodium-Ion Batteries," *Advanced Functional Materials* 33, no. 33 (2023): 2302200.

58. Z. Zhao, Y. Wu, R. Hu, et al., "Intercalation Pseudocapacitance in 2D VS_2/$Ti_3C_2T_x$ Mxene Hybrids for All-Climate and Long-Cycle Sodium-Ion Batteries," *Advanced Functional Materials* 33, no. 50 (2023): 2307794.

Supporting Information

Additional supporting information can be found online in the Supporting Information section.
Supporting_information.